Preprint of accepted manuscript for AGU Monograph on Tectonics of Alaska and Western Canada, 9/21/2023

Seismicity and Anisotropic Imaging Reveal an Active Detachment Beneath the Northern Alaska Range Foothills

Vera Schulte-Pelkum[1], Adrian Bender[2], and Natalia A. Ruppert[3]

[1]Cooperative Institute for Research in Environmental Sciences and Department of Geological Sciences, University of Colorado Boulder, Boulder, Colorado, USA
[2]United States Geological Survey, Alaska Science Center, Anchorage, Alaska, USA
[3]Alaska Earthquake Center, University of Alaska Fairbanks, Fairbanks, Alaska, USA

Abstract

North of the Denali Fault, the collision between the Yakutat block with North America is accommodated by a fold-thrust belt that gives rise to the northern Alaska Range foothills. At the western end of the belt, the Kantishna Hills anticline hosts prominent microseismicity and surface deformation, together interpreted as active folding of the Kantishna Hills anticline above a midcrustal detachment. Here, we test for such a detachment by using anisotropy-aware receiver functions to image fabric contrasts within the crust and comparing the depths of such contrasts to seismicity statistics. Seismic stations near the crest of the Kantishna Hills anticline and near its southern flank show a single strong contrast in dipping fabric at depths of 12 and 13 km, near where the microseismicity clusters at depth and consistent with a detachment plane beneath the fold. A minimum in b-value at 10-13 km depth is consistent with seismicity on the detachment, compatible with the imaged anisotropic contrast, while off-fault seismicity is shallower, deeper, and limited to smaller magnitudes. South-dipping imbricate thrusts in schist characterize the northern Alaska Range foothills structure and support our interpretation of the observed anisotropy as reflecting SSW–SSE-dipping foliation above a detachment at ~10–13 km depth that may exploit existing crustal weaknesses along more subtle fabric contrasts observed in the seismically quiescent region north of the actively deforming belt.

1 Introduction

Hundreds of kilometers north from Alaska's southern margin, Yakutat microplate collision and flat slab subduction drives crustal deformation of the continental interior (Fig. 1). Geodesy implies that near-margin shortening takes up ~80% of the contemporary 53 mm/yr north-northwest Yakutat-North America convergence (Elliott & Freymueller, 2020). Over 200 km inland, geologic right-lateral strike-slip approaching 15 mm/yr across the southeastern Denali Fault system takes up the remaining Yakutat velocity and decreases over ~350 km west along strike to ~5 m/kyr (= 5 mm/yr; Bender et al., 2023; Haeussler et al., 2017). This westward decrease in right-slip rate produces contraction and differential rock uplift north of the Denali Fault across the fold-thrust belt that gives rise to the northern Alaska Range foothills (Bemis et al., 2015; Haeussler et al., 2017; Matmon et al., 2006; Mériaux et al., 2009; Vallage et al., 2014).

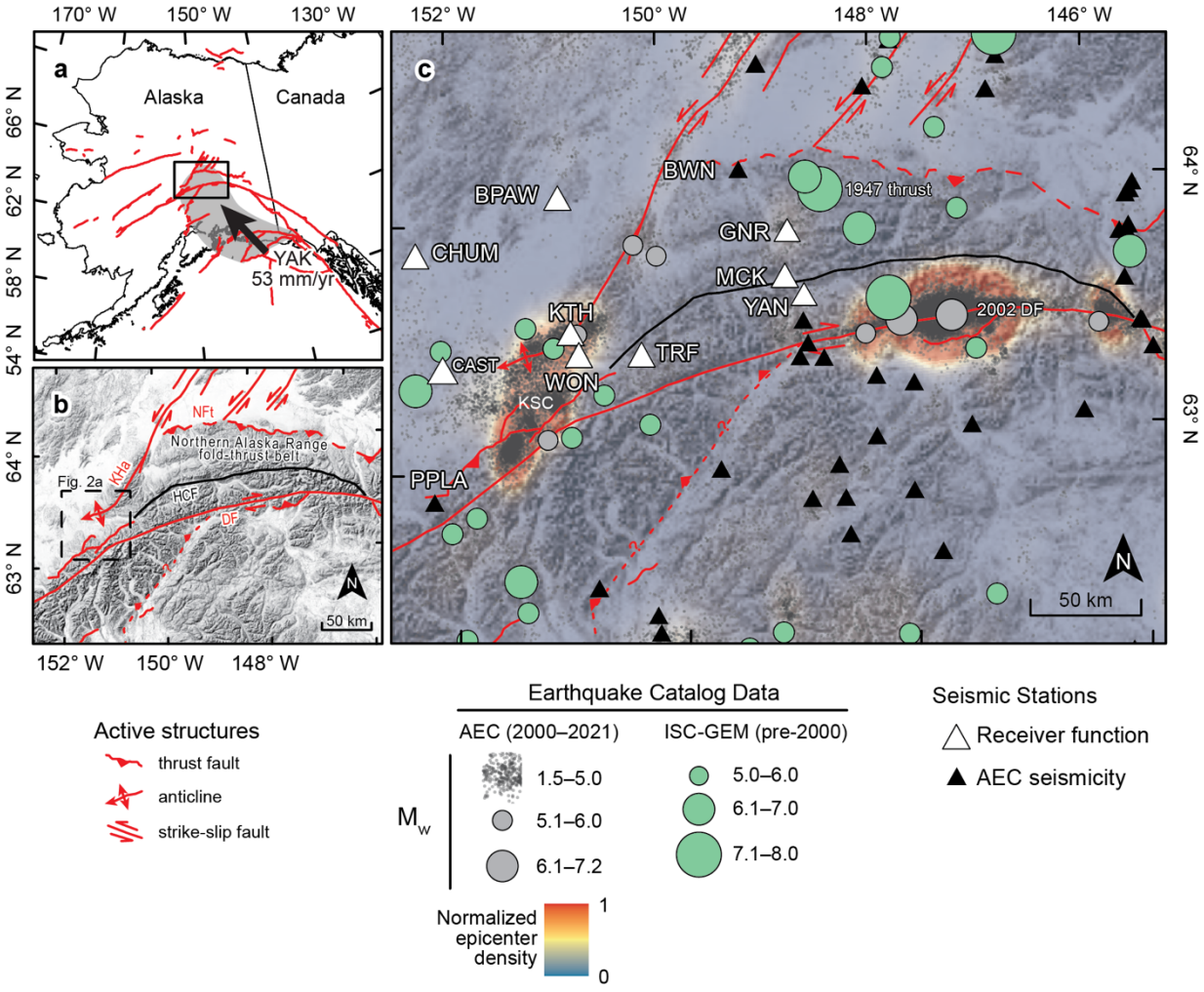

Figure 1. Study location and seismotectonic setting. (a) Location of the Northern Alaska Range fold-thrust belt (black box) in central Alaska. Yakutat microplate (YAK, grey shaded area) convergence rate from Elliott & Freymueller (2020). (b) The Northern Alaska Range fold-thrust belt. Simplified active structures are dashed where location is approximate, dashed and queried where both location and existence are uncertain. Dashed black box marks the location of Figure 2a. KHa—Kantishna Hills anticline; NFt—Northern Foothills thrust; DF—Denali Fault, HCF—Hines Creek Fault. (c) Seismicity and seismic stations of the Northern Alaska Range fold-thrust belt. Stations used in receiver function analysis in white (all from the AK network except for BEAAR stations WON, GNR, and YAN). Permanent stations used for Alaska Earthquake Center (AEC) relocations in black. Epicenter heat map rendered from AEC data recorded from 2000 to 2021 (AEC, 2023), International Seismological Center-Global Earthquake Model (ISC-GEM) epicenters plotted for pre-2000 events (Bondár et al., 2015). KSC—Kantishna seismic cluster. Base topography in (a) and (b) rendered from the U.S. Geological Survey (USGS) National Elevation Dataset 50 m resolution digital elevation model (https://tiles.arcgis.com/tiles/v01gqwM5QqNysAAi/arcgis/rest/services, last accessed 3 February 2023).

Geologic and geomorphic evidence indicate that the northern Alaska Range thrust belt accommodates far-field Yakutat convergence at 10^7–10^3-yr timescales. Inverted basin deposits capping the schist-cored fold and thrust belt (Bemis and Wallace, 2007; Wilson et al., 2015) imply the onset of north-vergent thrusting concurrent with the Oligocene-Miocene initiation of Yakutat collision (Ridgway et al., 2011). Structural interpretation places much of the fold-thrust belt above a south-dipping contractional detachment that ramps and shoals beneath the modern range front, where folded Pliocene-Pleistocene Nenana Gravel beds (ages constrained by Athey et al., 2006; Nørgaard et al., 2023) dip north consistent with Quaternary range front folding above a blind thrust (Bemis & Wallace, 2007). Rivers draining the range systematically steepen across the ~500 km-long range front (Lesh & Ridgway, 2007), consistent with ongoing fluvial adjustment to differential rock uplift (Kirby & Whipple, 2012), and warped landforms support interpretations of several mm/yr Quaternary shortening (Bemis, 2010).

The fold-thrust belt (herein referred to as thrust system) hosts considerable historical seismicity, including the 1947 M_w 7.1 Healy thrust earthquake sequence (St. Amand, 1948) (Fig. 1c). Likely because it occurred prior to recognition of the active northern Alaska Range thrust system (Bemis & Wallace, 2007; Ruppert et al., 2008), the 1947 event lacked geologic context (e.g., Page et al., 1995) and remained largely unexplored in subsequent neotectonic studies until recently (Bender et al., 2023). The 1947 mainshock likely involved ~5 m of blind co-seismic slip at 6±4 km depth (Fletcher & Christensen, 1996), though other estimates place the hypocenter at sub-Moho depths (e.g., Bondár et al., 2015). The epicenters map in the thrust system hanging wall (upper plate) near the range front as relocated in the International Seismological Center-Global Earthquake Model catalog (ISC-GEM; Bondár et al., 2015). In contrast, highly uncertain relocations by Doser & Baker (2023) place 1947 epicenters between the thrust system hanging wall at the range front and the low-relief Tanana basin to the north. Waveform inversion poorly constrains the 1947 event's mainshock thrust mechanism (Fletcher & Christensen, 1996), but Modified Mercalli Intensities indicate peak ground motion directed to the north (St. Amand, 1948), independently consistent with a south-dipping thrust source (cf. Bilham, 2019). In the 1947 epicentral zone, Bender et al. (2023) measured rates of river incision that increase northward from <1 mm/yr to ~5 mm/yr across the range-front anticline, and used northward GPS velocities to constrain a kinematic model involving a gently (~7°) south-dipping detachment that accords with low incision rates south of the range front and intersects the ~6 km mainshock hypocenter depth of Fletcher & Christensen (1996).

At the west end of the thrust system, copious microseismicity and several historical M_w 5+ earthquakes (1980, 1985, 2011; Bondár et al., 2015) occur beneath the Kantishna Hills anticline (Bender et al., 2019; Lesh & Ridgway, 2007). The microseismicity, mostly $M \leq 3$ events monitored since 1968 at steady rates, makes up three Kantishna seismic clusters between the anticline and the Denali Fault (Ratchkovski & Hansen, 2002; Ruppert et al., 2008). In these clusters, ~90% of events occur in the upper 12 km (Ruppert et al., 2008) of the locally 30+ km-thick crust (e.g., Berg et al., 2020; Miller et al., 2018). The seismicity appears diffuse in the Alaska Earthquake Center (AEC) catalog (Burkett et al., 2016) as well as when using double difference relocation (Burris, 2007). Beneath the Kantishna Hills anticline, northern Kantishna cluster focal mechanisms indicate primarily strike-slip and thrust faulting, with P-axes oriented north-northwest consistent with shortening associated with the west-southwest strike of the

overlying fold (Ratchkovski & Hansen, 2002).

Above the seismic cluster, the Kantishna Hills anticline accommodates active surface deformation. The fold is defined both topographically and structurally; foliations in Paleozoic Birch Creek schist define an anticline axis (Bundtzen et al., 1976) that matches the topographic fold crest above the northern Kantishna seismic cluster. Across the fold axis, dates of deeply incised river terraces imply up to ~1.4 mm/yr of differential bedrock incision since 22 ± 3 ka (Bender et al., 2019). Based on the maximum density of relocated small earthquake hypocenters on a strike-normal swath profile across the anticline (M<3; 7,710 events; interval 1988–2018), Bender et al. (2019) inferred a sub-horizontal contractional detachment at 10 ± 2 km depth beneath the fold. Assuming (1) conservation of mass (*sensu* Lavé & Avouac, 2000), and (2) that surface deformation and terrace incision result from simple hanging wall (upper plate) folding the above the seismicity-inferred detachment, Bender et al. (2019) computed ~1.2 mm/yr of north-directed late Pleistocene-averaged shortening across the Kantishna Hills anticline.

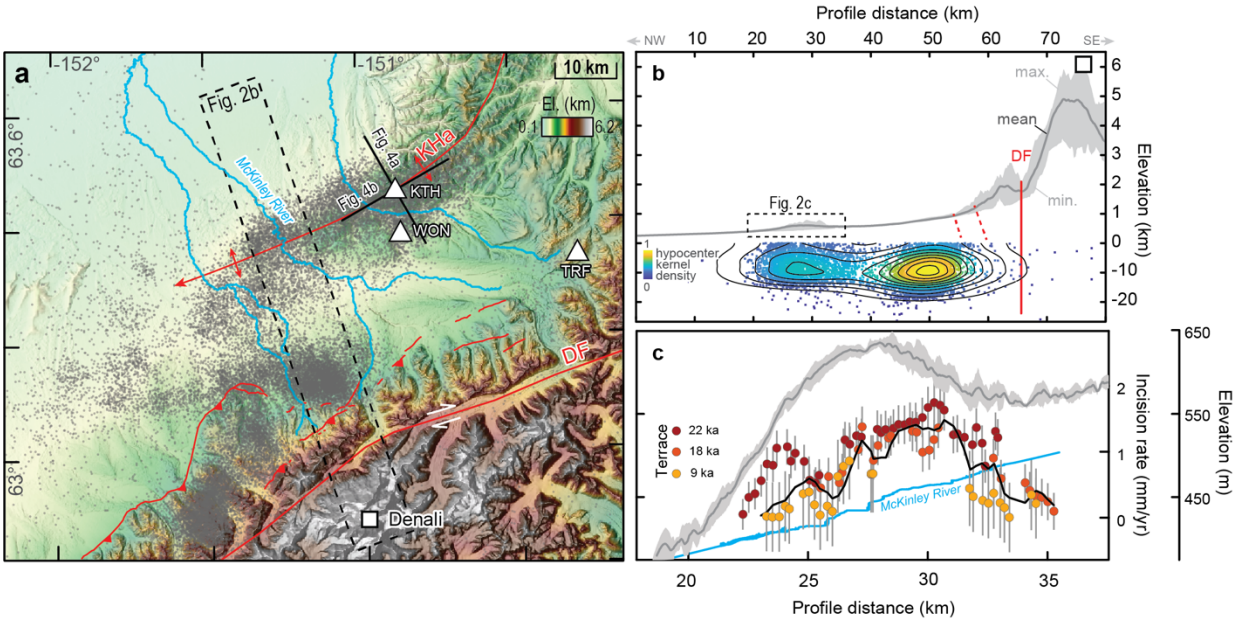

Figure 2. Morphotectonics of the Kantishna Hills anticline, modified from Bender et al. (2019). (a) Seismicity (grey dots) and topography (Alaska interferometric synthetic aperture radar; earthexplorer.usgs.gov) of the Kantishna Hills anticline (KHa) region north of the Denali Fault (DF) and North America's highest summit, Denali (white square). White triangles mark seismic stations, black lines locate profiles in Figure 4. (b) Swath profile of elevation and hypocenter depth within dashed box on Figure 2b. (c) Kantishna Hills anticline swath (grey envelope as in Figure 2b) and McKinley River elevation profile overlain with dated strath terrace-derived bedrock river incision rates and 5 km moving average (black line).

At present, the results of Bender et al. (2019, 2023) represent the only direct geologic rate constraint on Pleistocene northern Alaska Range thrust system deformation (cf. Bemis et al., 2015). In this setting, shortening rates are particularly valuable for understanding the distribution of ongoing far-field Yakutat microplate convergence-driven strain, of which ~5 mm/yr may be accommodated by slip on a basal detachment beneath the thrust system (Bender et al., 2023).

The Kantishna Hills shortening rate of Bender et al. (2019) relies on the presence of a inferred contractional detachment that is compatible in depth and geometry with the basal fault proposed by Bemis & Wallace (2007) and modeled by Bender et al. (2023) in the 1947 Mw 7.1 Healy earthquake epicentral region. Hence, a test of the detachment beneath the active Kantishna Hills anticline may have broader implications for the structure of the seismogenic northern Alaska Range thrust system.

Here, we test the inferred northern Alaska Range foothills detachment by placing observed seismicity in direct relation to crustal features from structural imaging. In the following, we use receiver functions to target contrasts in rock fabric within the crust. We compare the depth of an inferred structural contrast directly to that of seismicity by working in delay time space, avoiding distortion due to uncertainties in crustal velocity. We interpret the results in context with depth-dependent b-values for seismicity in terms of the proposed regional detachment.

2 Receiver function analysis of contrasts in anisotropy with depth

Data and processing

We use waveform data for stations from the Alaska permanent network (AK) located within our study area (Fig. 1) from 2000-2022, supplemented by temporary deployment data from the Broadband Experiment Across the Alaska Range (BEAAR) experiment in 1999-2001. Iterative time domain *Ps* receiver functions with a Gaussian filter parameter of 3 (corresponding to ~1 s pulse width for each arrival) are calculated for all events at epicentral distances of 28-150° with 5.0 or greater magnitude, resulting in an initial set of 312,156 radial and transverse component receiver functions. We apply automated quality control to this initial set, with selection criteria as described in detail in Schulte-Pelkum & Mahan (2014a) including P arrival signal-to-noise ratio, percent of the signal reproduced by convolution, initial P arrival polarity and amplitude, and pulse length. After quality control, 31,798 receiver functions are retained for analysis.

2.1 Harmonic analysis of arrivals from contrasts in anisotropy

Receiver functions in isotropic flat-layered media show arrivals on the radial component at times corresponding to the depth of contrasts in shear velocity (Langston, 1977; Phinney, 1964; Vinnik, 1977). The arrivals have positive polarity for a slow-over-fast contrast, negative for the opposite. The transverse component is zero in the flat-layered isotropic case. In our study area, stations show prominent arrivals that change polarity depending on the backazimuth of each teleseismic event. An example is shown in Fig. 3 for station KTH located atop the Kantishna Hills anticline. Fig. 3a shows radial component receiver functions binned by event backazimuth. In standard receiver function analysis, all individual event traces would be stacked to obtain, for example, the delay time and thus depth of the Moho, but Fig. 3a makes it clear that the waveforms depend on backazimuth. We stack the backazimuthally binned traces to obtain an estimate of the azimuthally invariant radial signal that is less biased by uneven azimuthal sampling caused by the distribution of teleseismic sources (green/yellow trace at top of Fig 3a

labeled R_0). The Moho is visible at ~3.7 s. The azimuthal section in Fig. 3a shows arrivals (e.g., at ~1.5 s) that change polarity depending on backazimuth, with an accompanying arrival on the transverse component (Fig. 3b; T_0 is zero even in the presence of dipping interfaces or anisotropy, but can be nonzero when the sensor is misoriented). Such behavior is characteristic of layers with P velocity anisotropy or dipping interfaces with isotropic velocity contrast (e.g., Levin & Park, 1997; Savage, 1998). In this case, we can exclude the dipping isotropic contrast case because of the lack of a polarity-reversed direct arrival (Schulte-Pelkum & Mahan, 2014a).

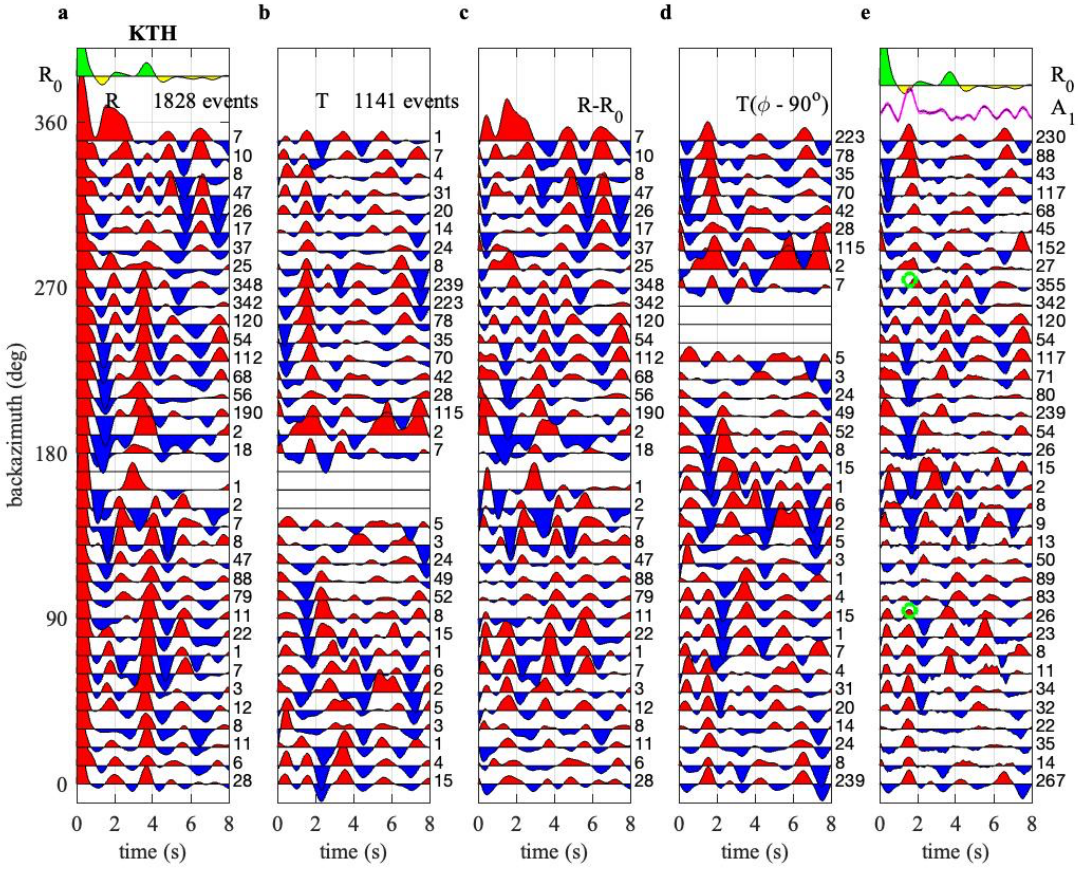

Fig. 3: Example of receiver function analysis at station KTH atop the Kantishna Hills anticline. (a) Radial component receiver functions. Red fill for positive, blue for negative polarity arrivals. Time is corrected for slowness so that delay time corresponds to vertical incidence. Amplitudes are corrected to a reference slowness of 0.06 s/km as in Jones and Phinney (1998). Traces are averaged in 10° backazimuthal bins; no azimuthal smoothing is applied. Numbers on right show the number of individual event-station traces stacked per bin. Green/yellow trace on top is the average of all azimuthal bin traces, R_0, a proxy for the azimuthally invariant signal. (b) as in a, but for transverse component. (c) Radial component traces with the azimuthal average subtracted from each bin trace. (d) Transverse component, now shifted by 90° in backazimuth to match c (rotating the system by +90° is equivalent to rotating the coordinates by -90°). (e) All individual traces from c and d binned together. Top trace A_1 is the first azimuthal harmonic amplitude (blue; bootstrap error bounds in magenta). Green circles are locations of polarity flips (strike of foliation) of the largest A_1 arrival. The time of the arrival corresponds to a depth of 12.8 km.

To isolate the azimuthally varying signal, we use a backazimuthal harmonic analysis as described in detail in Schulte-Pelkum and Mahan (2014a) and Schulte-Pelkum et al. (2020). We first subtract R_0 from each azimuthally binned trace in Fig. 3a and obtain Fig. 3c. Plunging axis anisotropy results in a first azimuthal harmonic arrival (polarity flips every 180°) with a 90° azimuthal phase shift between radial and transverse component (e.g., Jones & Phinney, 1998; Schulte-Pelkum & Mahan, 2014a, 2014b; Shiomi & Park, 2008), so we shift the transverse component traces by 90° in azimuth in Fig. 3d. The traces in panels Fig. 3c and d now display the same out-of-plane signal (Schulte-Pelkum & Mahan, 2014a). In order to increase the number of events per backazimuth bin, cover holes in azimuthal coverage thanks to the 90° shift in the transverse component, and amplify the first azimuthal harmonic, we stack corrected radial and transverse components together (Fig 3e) before solving for first (360° -periodic) backazimuthal harmonic amplitude in a moving time window. The amplitude of the first azimuthal harmonic (A_1, plotted on top of Fig. 3e in blue, with bootstrap error bounds in magenta) shows a peak at 1.59 s. Using the AEC's northern Alaska upper crustal velocity model values of Vp = 5.9 km/s and Vs = 3.3 km/s, this delay time corresponds to a depth of 12.8 km. The green circles in Fig. 3e denote the polarity flips in the first azimuthal harmonic fit and correspond to the strike of the foliation at the foliation contrast (Schulte-Pelkum et al., 2020), in this case ~E-W. The polarities are consistent with a south-dipping foliation above the contrast. A signal of comparable amplitude is found at temporary station WON (Fig. 2) at 13.8 km depth, with a strike closer to ENE-WSW. Both arrivals fall in a depth range similar to the peak in seismicity in Fig. 2, and we investigate their locations relative to seismicity in the next section.

3 S-minus-P delay time space comparison of seismicity depths with structural contrasts

The determination of the depth of local events as well as the time-to-depth scaling of receiver function arrivals is strongly dependent on compressional and shear velocities above the event or converting interface. Both types of depth determination rely on the time difference between P and S arrivals. For local seismicity, depth control is obtained from P and S picks; for receiver functions, depth is scaled from the time difference between the incident teleseismic P phase and converted S phase. An inaccurate velocity model can lead to significant mislocation in depth (Schulte-Pelkum et al., 2019). Depth distortion can be avoided by omitting the time-to-depth scaling altogether and working in S-P delay time (Schulte-Pelkum et al., 2019).

We consider events from 2020-2021 near station KTH, with hypocenters at a distance less than 0.15° (<17 km distance) from the station, a local magnitude Ml greater than 1.4, depths less than 30 km, and more than 20 phases from all reporting stations per event. We use events that have S and P picks at KTH. The times are corrected to vertical incidence using the catalogued depth, distance, and northern Alaska velocity model; any bias from the velocity model in this correction is much smaller than the corresponding bias when scaling to depth (Schulte-Pelkum et al., 2019). After correction to vertical incidence, the event S-P times are plotted as a function of hypocenter position along profiles in relationship to receiver function station positions and arrival times. Any location errors affecting the epicentral distance from the station would appear as a horizontal shift in the profiles. The effect of hypocenter errors on the correction to vertical incidence of the event S-P times is much smaller than depth errors from event locations

in a depth profile (Schulte-Pelkum et al., 2019).

Results are shown in Fig. 4. We compare the time (depth) and position of the A_1 arrival from the two stations on the anticline to those of all seismicity above Ml=1.4 and to larger events (Ml 2.5 or above) closer to KTH (within 10 km). The conversions and seismicity fall into a similar midcrustal depth range. The across-fold profile (Fig. 4a) shows clustering near KTH under the fold crest, while the along-fold profile in Fig. 4b shows seismicity that is more extended along the profile.

4 Frequency magnitude distribution (b-value) analysis

Frequency-magnitude distribution (FMD) of earthquakes or b-value has been used for characterizing properties of fault zones, aftershock sequences, swarms, and intraslab seismicity for decades. FMD can reveal patterns in distribution of events of certain sizes and differences in b-values reflect heterogeneity in properties of the subsurface structures. A b-value of 1 simply means that there are about 10 times more small events per magnitude decrease. High b-values are associated with prevalence of small earthquakes and a lack of large magnitude events, while low b-values indicate larger proportion of higher magnitude events than expected from a normal distribution. Variations in b-values have been correlated with state of stress, pore pressure, dehydration processes, and other rock conditions (Wiemer & Wyss, 2002).

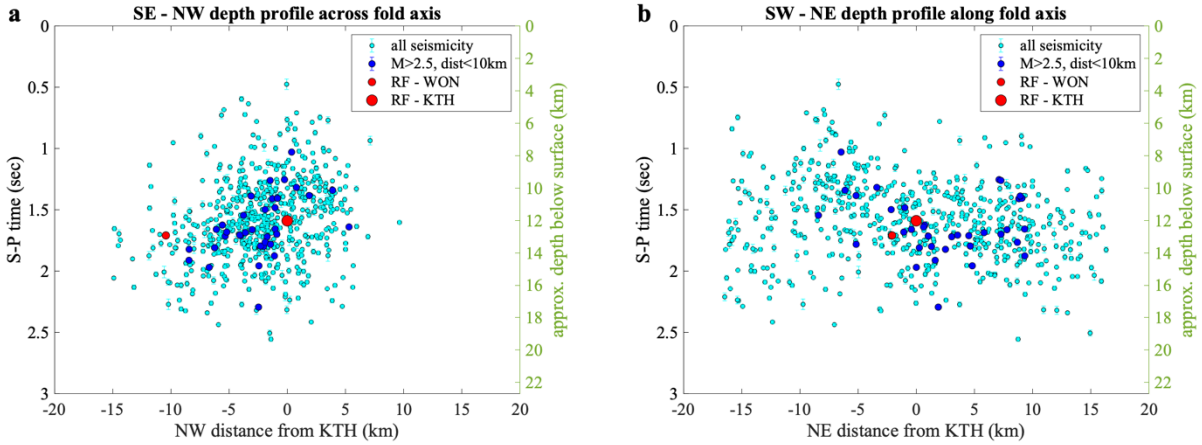

Fig. 4: S-P time profiles for seismicity near station KTH (Fig. 2). Locations of profiles a and b are shown in Fig. 2a. (a) Profile across the fold axis. Light and dark blue dots are seismicity with criteria as shown in the legend, plotted below the location of the hypocenter. Error bars (small) show the nominal pick time error. Green scale on the right shows approximate depth when scaled with the northern Alaska velocity model. Red dots are A_1 receiver function (RF) arrivals, plotted below the station location. (b) As in a, but for a profile along the fold axis.

We investigated b-value variations within the Kantishna cluster seismicity using the Matlab-based ZMAP statistical analysis package (Wiemer, 2001) and data from the AEC catalog recorded between 2000-2021. We used all available magnitudes (as low as 0) for the analysis and

investigated both regionalized and depth dependencies. The most significant patterns were revealed in mapping depth variations of FMD within the Kantishna cluster (over 35,000 events) and the anticline region (over 16,000 events). We computed b-values with a sliding window of 300 events. The magnitude of completeness (Mc) is computed for each sliding window and taken into account for the b-value calculation. Estimated Mc for the entire dataset is 0.9 and varies between 0.7 and 1.1 with depth when computed with a sliding window of 2 km (Fig. 5b). Hypocentral errors may introduce a bias to the b-value depth distribution. The large number of events per depth bin (Fig. 5c), overall location of the cluster in the upper to middle crust, and the long-term presence of local seismic stations, however, result in consistent and low location errors. Only about 5% of events have depth errors larger than 3 km, and the median and mean errors are less than1.0 and 1.5 km, respectively, for depths between about 3 and 20 km (Fig. 5b). Higher errors for depths below 20 km are due to the smaller number of events in each sample window resulting in the few events with higher errors introducing a larger bias into the mean and median values (Fig. 5c).

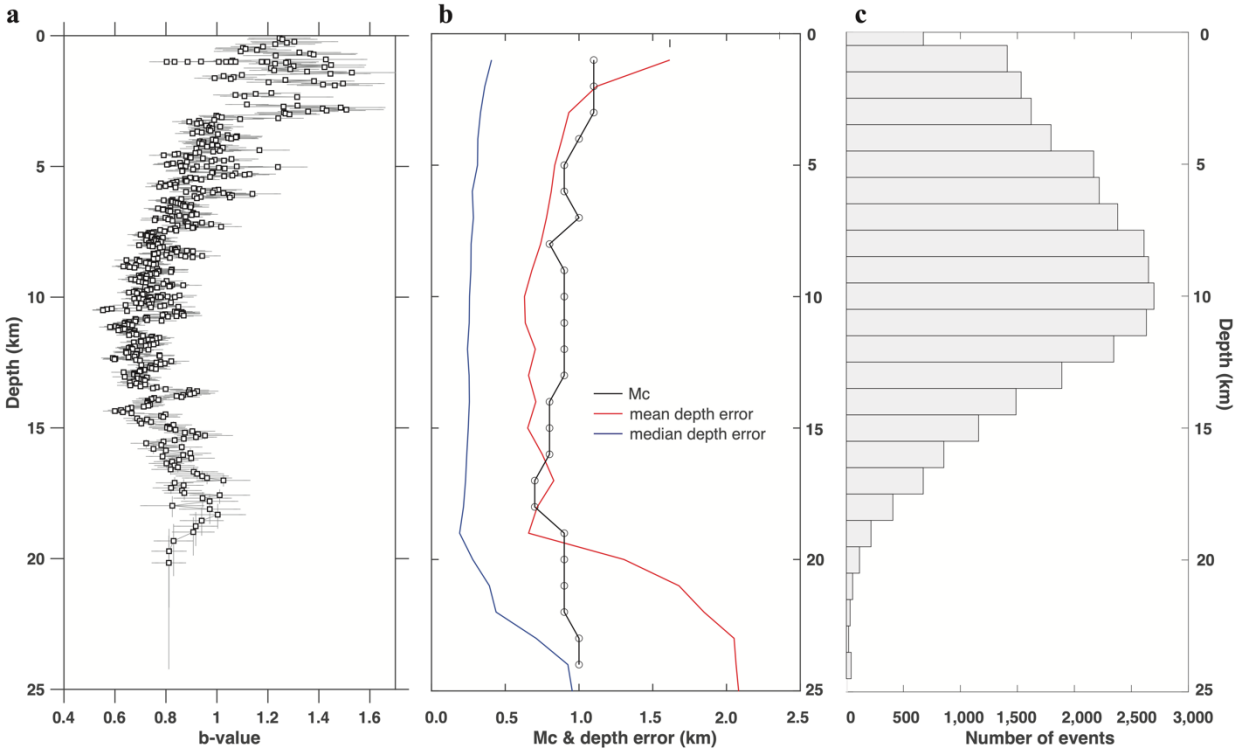

Fig. 5: (a) Depth profile for b-values for the Kantishna Hills cluster under the anticline. Depths are relative to sea level. b-values and errors are calculated with ZMAP (Wiemer, 2001). A sliding window over 300 events was used. (b) Magnitude of completeness (Mc) and depth error as functions of depth, calculated using a 2 km sliding depth window. (c) Histogram of depth distribution of events in the cluster. Note that bins down to 15 km depth contain over 1,000 events each.

5 Results

Two stations on the crest (KTH) and flank (WON) of the anticline show a peak in the first azimuthal harmonic (360° azimuthal period; A_1) at ~13-14 km, consistent with the depth of the concentration of seismicity (Fig. 4). The strike of the imaged foliation (Fig. 6) at the contrast is uniquely determined by this method and shows as parallel to the anticline crest (WON) or close to parallel to it (KTH). The phase of the A_1 polarity flips (negative amplitude arrivals from the south, positive from the north) has nonuniqueness in possible interpretations (Schulte-Pelkum et al., 2020) and requires that the contrast at this depth has either a more pronounced S-dipping foliation above it or a more pronounced N-dipping foliation below it. Surface exposures of schist with south-dipping foliation (e.g., Bundtzen et al., 1976) suggest that the former case may be more likely, with the converter being a fault contact between schists with south-dipping foliation above and a less anisotropic unit below. Midcrustal depth strikes observed at KTH, WON, and TRF are subparallel to foliation strikes mapped at the surface (Bundtzen et al., 1976). The same holds for the eastern stations, where receiver functions arrivals at GNR, MCK, and YAN show strikes that are approximately parallel to folds and related thrusts mapped at the surface (e.g., Bemis et al., 2012; Bemis & Wallace, 2007). While stations KTH and WON on the anticline and GNR in the northern part of the fold-thrust belt each show a single prominent A_1 arrival from the upper crust, stations TRF, MCK, and YAN have additional shallower arrivals (shown for YAN in Fig. 6b) that may stem from internal structure in the thrust wedge above the detachment.

Extending this analysis to stations in the wider region shows no pronounced midcrustal converters with anisotropic contrast in the area north and west of Kantishna Hills (Fig. 6). To the east, within the northern Alaska range fold-thrust belt, we observe deeper (19-25km; stations TRF, MCK, YAN) arrivals with similar amplitudes to those from stations KTH and WON near the anticline, in addition to some shallower arrivals at stations GNR and YAN, all with the same polarity sense (Fig. 6). Other stations show pronounced reverberations from soft near-surface layers that overprint any A_1 signals.

The strength of anisotropy can be estimated from the A_1 conversion amplitude. The latter depends on the anisotropic contrast at the converter, the incidence angle (which we correct to a common value), the dip angle of the foliation, and the geometry of the anisotropic tensor (Brownlee et al., 2017). In the hexagonal approximation, the last point is due to the variation of velocities in between the symmetry axis and the symmetry plane, usually described by a fifth anisotropic parameter η or η_κ (Brownlee et al., 2017; Kawakatsu, 2018). We use a crustal anisotropy database from rock sample observations (Brownlee, 2017) to estimate the strength of anisotropy. The observed A_1 signal strength of ~0.1 (Fig. 6a) horizontal to vertical component ratio can be generated by a minimum of 4-9% anisotropy (Brownlee et al., 2017) if the foliation dip is oriented optimally (intermediate to steep foliation plane dips of around 55° from horizontal) for the crustal rocks in the database. For much shallower or for nearly vertical dips, the anisotropy could be stronger. We note that the estimated strength of anisotropy need only exist in a 2-3 km thick layer above the detachment (Schulte-Pelkum and Mahan, 2014b), since the receiver function method is sensitive to contrasts in anisotropy rather than bulk anisotropy. If the anisotropy was limited to a discrete layer above the detachment, we would observe an opposite polarity arrival from its upper interface; this is not the case (Fig. 3). Endmember models

allowed by our observations have anisotropy that is continuous to the surface or gradually changes between the detachment and the surface.

S-P delay time analysis shows that the seismicity concentrates at about the same depth as that of the A_1 arrivals in receiver functions. Cross sections of the seismicity and receiver function arrivals show concentrated seismicity across the fold (Fig. 4a) and distributed seismicity along the fold (Fig. 4b).

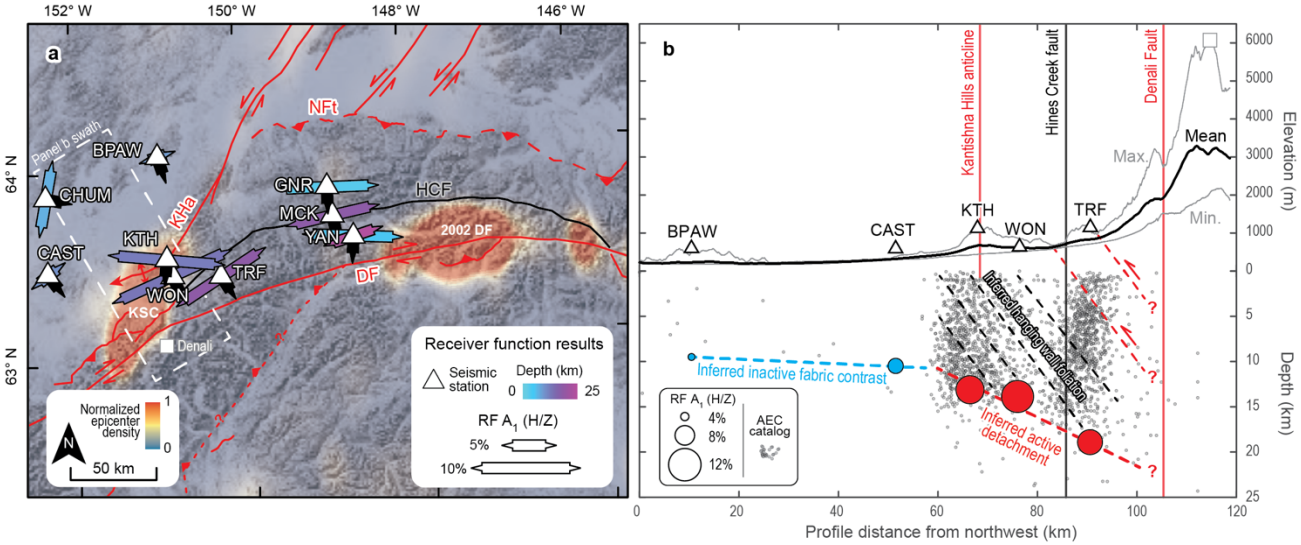

Figure 6. Receiver function results in morphotectonic context. (a) White triangles are station locations. Color-filled two-sided arrows show strike of the foliation at a contrast (e.g., azimuth of green circles in Fig. 3). Length of the double-sided arrow is scaled by the amplitude of the A_1 (Fig. 3e) arrival (see legend in inset). Black arrow points in downdip direction assuming that the contact is at the bottom of the layer with stronger anisotropy. White dashed box shows location of inset map on panel b. (b) Swath profile of landscape and seismic station elevation, hypocenter and receiver function converter depth (red dots), location of profile shown on inset map. Alaska Earthquake Center (AEC) catalog events (grey dots) within the dashed box are shown on the profile. Circles show amplitude and depth of A1 receiver function conversions, shown in red for inferred active detachment and blue for inactive contact. Red dashed line represents the detachment we infer from receiver function (RF) contrast depths, black dashed lines represent south-dipping hanging wall foliation that may explain the contrast in anisotropy across the inferred detachment. SD—standard deviation of elevation swath.

Analysis of b-values shows a minimum in the 11-13 km depth range. Results for the entire Kantishna cluster and just the northern part that includes the Kantishna anticline area (Fig. 5) are similar. The values in the shallower range (0-5 km) are the highest and generally over 1, then start to gradually decrease below 5 km, and once again increase below 15 km depth. We find that the lowest b-values (0.6-0.7) are observed in the 11-13 km depth range (Fig. 5), at the depth of the inferred detachment. We interpret the minimum as being related to the detachment zone localized at this depth, where larger earthquakes that contribute to the observed surface deformation mostly occur. Higher b-values especially above and possibly also below the detachment zone may reflect diffuse hanging wall and foot wall deformation manifested by smaller earthquakes.

6 Discussion

Our receiver function analysis indicates an active detachment beneath the Kantishna Hills anticline broadly consistent with that proposed by Bender et al. (2019). In contrast with their hypothesized 10±2 km-deep (relative to sea level) sub-horizontal detachment (Fig. 2b), our results imply a detachment at depths (relative to station elevations) that increase southward from the anticline over ~25 km distance (Fig. 6). We image a candidate detachment 12.8 km below station KTH positioned at the surface of the anticlinal crest, 13.8 km beneath WON south of the anticline, and 18.9 km beneath TRF southeast of the fold and related seismic cluster (i.e., 11.6, 13.1, and 17.2 km below sea level, respectively). Projected onto a strike-normal profile across the Kantishna Hills anticline, these results indicate a detachment that strikes ~060° and dips 12–13° south toward the Denali Fault. Using our refined detachment depth of 11.6 km (relative to sea level) beneath the anticline, and the uplifted terrace areas and ages of Bender et al. (2019), we calculate 0.7–1.5 mm/yr of shortening across the Kantishna Hills anticline, overlapping the ~1.2 mm/yr of shortening reported by Bender et al. (2019).

Regionally, we observe similar fabric contrasts from receiver functions that extend to somewhat greater depths (up to ~25 km) to the east in the northern Alaska Range fold-thrust belt (e.g., stations TRF and MCK; Fig. 6). Two temporary BEAAR stations in the thrust belt (GNR, YAN) yield shallower converter depths at 3-4 km. At station YAN, there is also a deeper (~25 km), smaller amplitude A_1 arrival with strike aligned with the fold and thrust belt. Shallower arrivals with strikes aligned with the thrust belt may mark fabric contrasts within the thrust wedge compatible with secondary faulting and folding within the thrust sheet (e.g., Bemis et al., 2012) or lithologic changes in the metamorphic rock assemblages that core the thrust system (e.g., intercalated schists and gneisses of varying compositions and structure; Dusel-Bacon et al., 2016; Forbes & Weber, 1970; Wahrhaftig & Black, 1958).

The extent, geometry, and depth of the detachment imaged beneath the Kantishna Hills anticline compares well with fold-thrust belt theory (e.g., Dahlen, 1990; Dahlen et al., 1984; Suppe, 2007) and global observations (e.g., Lacombe & Mouthereau, 2002; Pfiffner, 2017). In a cross section spanning our study area, the northern Alaska Range thrust belt forms a north-tapering wedge (Fig. 2b), defined by north-sloping topography at the surface and the gently south-dipping detachment imaged at mid-crustal depths between the Denali Fault to the south and the Kantishna Hills anticlinal deformation front to the north (Fig. 2b). This configuration matches expectations of critically tapered fold-thrust belts with internal competence exceeding that of an underlying weak, low-angle detachment fault that dips opposite to the vergence direction and topographic slope of the deforming region (Suppe, 2007). Such detachments are thought to form under even relatively low tectonic stresses along some combination of pre-existing crustal weakness (i.e., faults or lithologic competency contrasts) and depth-related (i.e., thermal, mechanical, rheologic) changes in crustal strength (e.g., Dahlen, 1990; Lacombe & Mouthereau, 2002).

Whether the Kantishna detachment produces or results from a contrast in rock fabric remains uncertain. Where observed, rocks beneath basal thrust belt detachments are commonly minimally deformed relative to the overlying inner wedge (e.g., Dahlen, 1990). While direct observation of rock fabric contrasts across the detachment beneath Kantishna Hills anticline (e.g., in drill core)

is not currently possible, we suggest that such a contrast forms the receiver function converter imaged at depth herein. Consistent with receiver function results across the Kantishna Hills anticline, we suggest that the contrast may reflect south-dipping foliation and secondary faults developed within the hanging wall due to northward transport on the detachment that truncates the internal hanging wall fabric. This scenario implies that the receiver functions image an anisotropy contrast intrinsically linked to recent and ongoing deformation, as opposed to anisotropy changes purely associated with lithologic variations within the Paleozoic Birch Creek schist that underlies both the actively deforming Kantishna Hills and the tectonically quiescent region to the west (Fig. 6). In accord with this interpretation, the inferred detachment cross-cuts the Cretaceous Hines Creek fault (Fig. 6), which marks the contact between schists to the north and suture zone rocks to the south (Wahrhaftig et al., 1975).

Strong receiver function signal amplitudes at stations in the deforming region (Fig. 6a; KTH, WON, TRF, GNR, MCK, YAN) compared to the small amplitudes at stations outside the anticline and thrust belt (CAST, CHUM, BPAW) indicate that the strength of the contrast is related to active deformation. Of particular interest in this comparison are stations CAST and BPAW, situated on bedrock highs respectively mapped as Paleozoic Birch Creek schist (which also cores the active Kantishna Hills anticline ~20 km to the east) and Cambrian argillite intruded by Cretaceous granite (Wilson et al., 2015). The stations show arrivals from 10.5 km (CAST) and 9.5 km (BPAW) depth below the surface that strike NE-SW and dip SE, similar to stations on the anticline and in the thrust belt, but with much smaller amplitudes (Fig. 6a, b). Unlike the A_1 amplitudes of 10–12% across the actively deforming western thrust belt (i.e., KTH, WON, TRF), weaker conversions occur at CAST and BPAW with amplitudes of 7% and 3%, respectively. We propose that, relative to the more subtle fabric contrast imaged beneath CAST at depths comparable to but shallower than the Kantishna detachment, the active detachment may strengthen an existing fabric contrast, perhaps between the foliated and secondarily faulted schist in the hanging wall and less anisotropic rock in the footwall, or an anisotropy contrast between the hanging wall and the detachment itself (provided a minimum detachment thickness of ~2 km and a gradual transition above it). Although the broad, 60–80 km spacing between CAST and BPAW to the north and KTH on the Kantishna Hills anticline crest precludes precisely locating the blind detachment tip, the implicit absence of an active detachment implies that the co-located anticline and Kantishna seismic cluster mark the deformation front at northern extent of the thrust belt's northward propagation into the Minchumina basin.

The mechanism by which this fabric contrast amplification in the active detachment occurs during deformation remains unclear. We expect that northward transport of the Kantishna Hills hanging wall anticline should produce a south-dipping fabric in the fold core. Prevalent seismicity within the hanging wall above the hypothesized detachment depth, however, implies brittle internal deformation with uncertain implications for the development of seismically anisotropic fabrics. In accord with this scenario, the diffuse, high-frequency and relatively low-magnitude seismicity that occurs mostly above the receiver function-imaged detachment (Fig. 2a–b) likely reflects ongoing internal brittle deformation of the northern Alaska Range thrust belt due to continued far-field Yakutat microplate convergence (e.g., Eberhart-Phillips et al., 2006; Haeussler et al., 2017). The drop-off in seismicity beneath the imaged detachment in turn may represent minimal active deformation of rock beneath the inferred fault (Fig. 2b). With the

available evidence, however, we cannot rule out a detachment origin attributable to lithologic variations in a complex metamorphic assemblage (e.g., Wahrhaftig & Black, 1958) or other faults at depth.

7 Conclusions

We combined seismicity, receiver function analysis of azimuthally varying arrivals, and b-values on and around the actively deforming Kantishna Hills anticline. Results indicate an active detachment structure with abundant seismicity that dips gently south toward the Denali Fault. A minimum in b-value at the depth of the inferred detachment is consistent with a higher probability of larger magnitude events near the detachment, in contrast to seismicity limited to very small magnitudes above and below the detachment. We interpret the receiver function results as indicating a contrast in rock fabric that juxtaposes hanging wall schist with a south-dipping fabric atop a less anisotropic unit below the detachment. Deeper arrivals to the east may be a continuation of the same detachment structure in the more mature fold-thrust belt. To the west and north of Kantishna Hills, a lack of corresponding receiver function signal is interpreted as the absence of a detachment fault, consistent with the mapped extent of late Pleistocene surface deformation and contemporary seismicity.

Acknowledgments
This research was funded in part by National Science Foundation grants EAR-1927246 and 2049743. IRIS Data Services are funded through the Seismological Facilities for the Advancement of Geoscience and EarthScope (SAGE) Proposal of the National Science Foundation (NSF) under Cooperative Agreement EAR-1261681. We thank the operators and field teams of the AK (Alaska Earthquake Center, 1987) and BEAAR (Christensen et al., 1999) networks. We also thank editor Margarete Jadamec, two anonymous reviewers, Aaron Wech, Jonathan Caine, Thorsten Becker, and Charles Bacon for reviews, feedback, and discussions that improved the paper.

Availability Statement
IRIS Data Services (IRIS Data Management Center) provided access to waveforms and related metadata used in this study (https://doi.org/10.7914/SN/AK and https://doi.org/10.7914/SN/XE_1999). Data were retrieved via SOD (Owens et al., 2004). The seismicity catalog is available at https://earthquake.alaska.edu/earthquakes.

References

Athey, J., Newberry, R., Werden, M., Freeman, L., Smith, R., & Szumigala, D. (2006). Bedrock geologic map of the Liberty Bell area, Fairbanks A-4 Quadrangle, Bonnifield mining district, Alaska. In *Alaska Division of Geological & Geophysical Surveys Report of Investigation RI2006: Vol. 1.0.1.* https://doi.org/https://doi.org/10.14509/15026

Bemis, S. P. (2010). *Moletracks Scarps to Mountains: Quaternary Tectonics of the Central Alaska Range* [Doctoral dissertation, University of Oregon]. https://scholarsbank.uoregon.edu/xmlui/bitstream/handle/1794/10563/Bemis_Sean_Patrick_phd201

0win.pdf?isAllowed=y&sequence=1

Bemis, S. P., Carver, G. A., & Koehler, R. D. (2012). The Quaternary thrust system of the northern Alaska Range. *Geosphere*, *1*, 196–205. https://doi.org/10.1130/GES00695.1

Bemis, S. P., & Wallace, W. K. (2007). Neotectonic framework of the north-central Alaska Range foothills. *The Geological Society of America Special Paper 431*, *2431*(21), 549–572. https://doi.org/10.1130/2007.2431(21)

Bemis, S. P., Weldon, R. J., & Carver, G. A. (2015). Slip partitioning along a continuously curved fault: Quaternary geologic controls on Denali fault system slip partitioning, growth of the Alaska Range, and the tectonics of south-central Alaska. *Lithosphere*, *3*, 235–246. https://doi.org/10.1130/L352.1

Bender, A. M., Lease, R. O., Haeussler, P. J., Rittenour, T. M., Corbett, L. B., Bierman, P. R., & Caffee, M. W. (2019). Pace and process of active folding and fluvial incision across the Kantishna Hills anticline, central Alaska. *Geophysical Research Letters*, *46*(6), 3235–3244. https://doi.org/10.1029/2018GL081509

Bender, A. M., R. O. Lease, T. Rittenour, J. V. Jones (2023). Rapid active thrust faulting at the northern Alaska Range front. *Geology* 51 (6), 527–531. doi: https://doi.org/10.1130/G51049.1

Berg, E. M., Lin, F., Allam, A., Schulte-Pelkum, V., Ward, K. M., & Shen, W. (2020). Shear Velocity Model of Alaska Via Joint Inversion of Rayleigh Wave Ellipticity, Phase Velocities, and Receiver Functions Across the Alaska Transportable Array. *Journal of Geophysical Research: Solid Earth*, *125*(2). https://doi.org/10.1029/2019JB018582

Bilham, R. (2019). Himalayan earthquakes: A review of historical seismicity and early 21st century slip potential. *Geological Society Special Publication*, *483*(1), 423–482. https://doi.org/10.1144/SP483.16

Bondár, I., Engdahl, E. R., Villaseñor, A., Harris, J., & Storchak, D. (2015). ISC-GEM: Global Instrumental Earthquake Catalogue (1900-2009), II. Location and seismicity patterns. *Physics of the Earth and Planetary Interiors*, *239*, 2–13. https://doi.org/10.1016/j.pepi.2014.06.002

Brownlee, S. J., V. Schulte-Pelkum, A. Raju, K. Mahan, C. Condit, and O. F. Orlandini (2017). Characteristics of deep crustal seismic anisotropy from a compilation of rock elasticity tensors and their expression in receiver functions. *Tectonics*, 36, 1835–1857, https://doi.org/10.1002/2017TC004625.

Bundtzen, T.K., Smith, T.E., and Tosdal, R.M. (1976). Progress report: Geology and mineral deposits of the Kantishna Hills, Alaska: Alaska Division of Geological & Geophysical Surveys Alaska Open-File Report 98, 82 p., 2 sheets, scale 1:63,360. https://doi.org/10.14509/194.

Burkett, C. A., Bemis, S. P., & Benowitz, J. A. (2016). Along-fault migration of the Mount McKinley restraining bend of the Denali fault defined by late Quaternary fault patterns and seismicity, Denali National Park & Preserve, Alaska. *Tectonophysics*, 693, Part B, 489–506. https://doi.org/10.1016/j.tecto.2016.05.009.

Burris, L. (2007). Seismicity and stresses in the Kantishna seismic cluster, central Alaska, University of Alaska Fairbanks, M.Sc. thesis, https://scholarworks.alaska.edu/handle/11122/11069.

Dahlen, F. A. (1990). Critical taper model of fold-and-thrust belts and accretionary wedges. *Annual Review of Earth & Planetary Sciences*, *18*, 55–99. https://doi.org/10.1146/annurev.ea.18.050190.000415

Dahlen, F. A., Suppe, J., & Davis, D. (1984). Mechanics of Fold-and-Thrust Belts and Accretionary Wedges' Cohesive Coulomb Theory. *Journal of Geophysical Research*, *89*(B12), 87–101.

Dusel-Bacon, C., C. R. Bacon, P. B. O'Sullivan, W. C. Day (2016), Apatite fission-track evidence for regional exhumation in the subtropical Eocene, block faulting, and localized fluid flow in east-

central Alaska. *Canadian Journal of Earth Sciences* 53, 260-280,https://doi.org/10.1139/cjes-2015-0138

Eberhart-Phillips, D., Christensen, D. H., Brocher, T. M., Hansen, R., Ruppert, N. A., Haeussler, P. J., & Abers, G. A. (2006). Imaging the transition from Aleutian subduction to Yakutat collision in central Alaska, with local earthquakes and active source data. *Journal of Geophysical Research: Solid Earth*, *111*(11). https://doi.org/10.1029/2005JB004240

Elliott, J. L., & Freymueller, J. T. (2020). A Block Model of Present - Day Kinematics of Alaska and Western Canada. *Journal of Geophysical Research*, 1–30. https://doi.org/10.1029/2019JB018378

Fletcher, H. J., & Christensen, D. H. (1996). A Determination of Source Properties of Large Intraplate Earthquakes in Alaska. *Pure and Applied Geophysics*, *146*(1), 21–41. https://doi.org/https://doi.org/10.1007/BF00876668

Forbes, R. B. and F. R. Weber (1975). Progressive metamorphism of schists recovered from a deep drill hole near Fairbanks, Alaska. *Journal of Research of the U.S. Geological Survey* 3, 647-657.

Haeussler, P. J., Matmon, A., Schwartz, D. P., & Seitz, G. G. (2017). Neotectonics of interior Alaska and the late Quaternary slip rate along the Denali fault system. *Geosphere*, *13*(5), 1–19. https://doi.org/10.1130/GES01447.1

Jones, C. H., & Phinney, R. A. (1998). Seismic structure of the lithosphere from teleseismic converted arrivals observed at small arrays in the southern Sierra Nevada and vicinity, California. *Journal of Geophysical Research*, *103*(B5), 10065–10090.

Kawakatsu, H. (2018). A new fifth parameter for transverse isotropy III: Reflection and transmission coefficients. *Geophysical Journal International* 213(1), 426–433, https://doi.org/10.1093/gji/ggy003

Kirby, E., & Whipple, K. X. (2012). Expression of active tectonics in erosional landscapes. *Journal of Structural Geology*, *44*, 54–75. https://doi.org/10.1016/j.jsg.2012.07.009

Lacombe, O., & Mouthereau, F. (2002). Basement-involved shortening and deep detachment tectonics in forelands of orogens Insights.pdf. *Tectonics*, *21*(4). https://doi.org/10.1029/2001TC901018

Langston, C. A. (1977). The effect of planar dipping structure on source and receiver responses for constant ray parameter. *Bulletin of the Seismological Society of America*, *67*(4), 1029–1050. https://doi.org/10.1785/BSSA0670041029

Lavé, J., & Avouac, J. P. (2000). Active folding of fluvial terraces across the Siwaliks Hills, Himalayas of central Nepal. *Journal of Geophysical Research: Solid Earth*, *105*(B3), 5735–5770. https://doi.org/10.1029/1999jb900292

Lesh, M. E., & Ridgway, K. D. (2007). Geomorphic evidence of active transpressional deformation in the Tanana foreland basin, south-central Alaska. In K. D. Ridgway, J. M. Trop, J. M. G. Glen, & J. M. O'Neill (Eds.), *Tectonic Growth of a Collisional Continental Margin: Crustal Evolution of Southern Alaska: Geological Society of America Special Paper 431* (Vol. 2431, Issue 22, pp. 573–592). The Geological Society of America. https://doi.org/10.1130/2007.2431(22).

Levin, V., & Park, J. (1997). P-SH conversions in a flat-layered medium with anisotropy of arbitrary orientation. *Geophys. J. Int.* 131, 253-266.

Matmon, A., Schwartz, D. P., Haeussler, P. J., Finkel, R. C., Lienkaemper, J., Stenner, H. D., & Dawson, T. E. (2006). Denali fault slip rates and Holocene – late Pleistocene kinematics of central Alaska. *Geology*, *8*, 645–648. https://doi.org/10.1130/G22361.1

Mériaux, A.-S., Sieh, K., Finkel, R. C., Rubin, C. M., Taylor, M. H., Meltzner, A. J., & Ryerson, F. J. (2009). Kinematic behavior of southern Alaska constrained by westward decreasing postglacial slip rates on the Denali Fault, Alaska. *Journal of Geophysical Research*, *114*, 1–19. https://doi.org/10.1029/2007JB005053

Miller, M. S., O'Driscoll, L. J., Porritt, R. W., & Roeske, S. M. (2018). Multiscale crustal architecture of Alaska inferred from P receiver functions. *Lithosphere*, *10*(2), 267–278. https://doi.org/10.1130/L701.1

Nørgaard, J., Jansen, J. D., Neuhuber, S., & Knudsen, M. F. (2023). P – PINI : A cosmogenic nuclide burial dating method for landscapes undergoing non-steady erosion. *Quaternary Geochronology*, *74*. https://doi.org/10.1016/j.quageo.2022.101420

Owens, T., Crotwell, P., Groves, C., & Oliver-Paul, P. (2004). SOD: Standing order for data. *Seismological Research Letters*, *75*(4), 515–520.

Page, R. A., Plafker, G., & Pulpan, H. (1995). Block rotation in east-central Alaska: a framework for evaluating earthquake potential? *Geology*, *23*(7), 629–632. https://doi.org/10.1130/0091-7613(1995)023<0629:BRIECA>2.3.CO;2

Pfiffner, O. A. (2017). Thick-skinned and thin-skinned tectonics: A global perspective. *Geosciences (Switzerland)*, *7*(3). https://doi.org/10.3390/geosciences7030071

Phinney, R. A. (1964). Structure of the Earth's crust from spectral behavior of long-period body waves. *Journal of Geophysical Research*, *69*(14), 2997–3017. https://doi.org/10.1029/jz069i014p02997

Ratchkovski, N. A., & Hansen, R. A. (2002). New Constraints on Tectonics of Interior Alaska : Earthquake Locations, Source Mechanisms, and Stress Regime. *Bulletin of the Seismological Society of America* 92(3), 998–1014.

Ridgway, K. D., Trop, J. M., & Finzel, E. S. (2011). Modification of continental forearc basins by flat-slab subduction processes: a case study from southern Alaska. In C. Busby & A. Azor (Eds.), *Tectonics of Sedimentary Basins: Recent Advances* (pp. 327–346). https://doi.org/10.1002/9781444347166.ch16

Ruppert, N. A., Ridgway, K. D., Freymueller, J. T., Cross, R. S., & Hansen, R. A. (2008). Active Tectonics of Interior Alaska: Seismicity, GPS Geodesy, and Local Geomorphology. In J. T. Freymueller, P. J. Haeussler, R. Wesson, & G. Ekstron (Eds.), *Active Tectonics and Seismic Potential of Alaska, Geophysical Monograph Series 179*. American Geophysical Union. https://doi.org/10.1029/179GM06

Savage, M. K. (1998). Lower crustal anisotropy or dipping boundaries? Effects on receiver functions and a case study in New Zealand. *Journal of Geophysical Research: Solid Earth*, *103*(B7), 15069–15087. https://doi.org/10.1029/98JB00795

Schulte-Pelkum, V., & Mahan, K. H. (2014a). A method for mapping crustal deformation and anisotropy with receiver functions and first results from USArray. *Earth and Planetary Science Letters*, *402*(C), 221–233. https://doi.org/10.1016/j.epsl.2014.01.050

Schulte-Pelkum, V., & Mahan, K. H. (2014b). Imaging Faults and Shear Zones Using Receiver Functions. *Pure and Applied Geophysics*, *171*(11), 2967–2991. https://doi.org/10.1007/s00024-014-0853-4

Schulte-Pelkum, V., Monsalve, G., Sheehan, A. F., Shearer, P., Wu, F., & Rajaure, S. (2019). Mantle earthquakes in the Himalayan collision zone. *Geology*, *47*(9), 815–819. https://doi.org/10.1130/G46378.1

Schulte-Pelkum, V., Ross, Z. E., Mueller, K., & Ben-Zion, Y. (2020). Tectonic Inheritance With Dipping Faults and Deformation Fabric in the Brittle and Ductile Southern California Crust. *Journal of Geophysical Research: Solid Earth*, *125*(8). https://doi.org/10.1029/2020JB019525

Shiomi, K., & Park, J. (2008). Structural features of the subducting slab beneath the Kii Peninsula, central Japan: Seismic evidence of slab segmentation, dehydration, and anisotropy. *Journal of Geophysical Research: Solid Earth*, *113*(10). https://doi.org/10.1029/2007JB005535

Sortor, R. N, B. M. Goehring, S. P. Bemis, C. A. Ruleman, M. W. Caffee, D. J. Ward (2015). Early Pleistocene climate-induced erosion of the Alaska Range formed the Nenana Gravel. *Geology* 49 (12), 1473–1477, https://doi.org/10.1130/G49094.1

St. Amand, P. (1948). The Central Alaska Earthquake Swarm of October 1947. *Transactions, American Geophysical Union*, *29*(5). https://doi.org/doi/pdf/10.1029/TR029i005p00613

Suppe, J. (2007). Absolute fault and crustal strength from wedge tapers. *Geology* 35 (12), 1127–1130. https://doi.org/10.1130/G24053A.1

Vallage, A., Devès, M. H., Klinger, Y., King, G. C. P., & Ruppert, N. A. (2014). Localized slip and distributed deformation in oblique settings: The example of the Denali fault system, Alaska. *Geophysical Journal International*, *197*(3), 1284–1298. https://doi.org/10.1093/gji/ggu100

Vinnik, L. P. (1977). Detection of waves converted from P to SV in the mantle. In *Physics of the Earth and Planetary Interiors* (Vol. 15). https://doi.org/10.1016/0031-9201(77)90008-5

Wahrhaftig, C., & Black, R. (1958). Quaternary and Engineering Geology in the Central Part of the Alaska Range. *Geological Survey Professional Paper 293*, 1–127. https://docs.google.com/uc?id=0B2Sg-tJFik5pbHhVOW0wTnpNVUU&export=download

Wahrhaftig, C., D. L. Turner, F. R. Weber, T. E. Smith (1975). Nature and timing of movement on Hines Creek strand of Denali fault system, Alaska. *Geology* 3 (8), 463–466. doi: https://doi.org/10.1130/0091-7613(1975)3<463:NATOMO>2.0.CO;2

Wiemer, S. (2001). A Software Package to Analyze Seismicity: ZMAP. *Seismological Research Letters*, *72*(3), 373–382. https://doi.org/10.1785/gssrl.72.3.373

Wiemer, S., & Wyss, M. (2002). Mapping spatial variability of the frequency-magnitude distribution of earthquakes. *Advances in Geophysics*, *45*, 259–302.

Wilson, F. H., Hults, C. P., Mull, C. G., & Karl, S. M. (2015). *Geologic map of Alaska: U.S. Geological Survey Scientific Investigations Map 3340*.